

Group Pre-processing in J1611+4026: Minor Rejuvenation of a Massive ETG fueled by Interaction-driven Gas Transfer

Yaosong Yu (于耀淞)¹ *, Qihang Chen (陈启航)^{2,3} , Zizhao He (何紫朝)^{4,5,6} , Limeng Deng (邓力猛)^{7,8} ,
Liang Jing (荆亮)^{2,3} , and Jianhui Lian (连建辉)¹ **

¹ South-Western Institute for Astronomy Research, Yunnan University, Kunming 650500, China

² School of Physics and Astronomy, Beijing Normal University, Beijing 100875, China

³ Institute for Frontier in Astronomy and Astrophysics, Beijing Normal University, Beijing, 102206, China

⁴ Department of Physics, Nanchang University, Nanchang, 330031, China

⁵ Center for Relativistic Astrophysics and High Energy Physics, Nanchang University, Nanchang, 330031, China

⁶ Purple Mountain Observatory, Chinese Academy of Sciences, Nanjing, Jiangsu, 210023, China

⁷ Technical University of Munich, TUM School of Natural Sciences, Physics Department, James-Franck-Straße 1, 85748 Garching, Germany

⁸ Max Planck Institute for Astrophysics, Karl-Schwarzschild-Straße 1, 85748 Garching, Germany

Received xxxx; accepted xxxx

ABSTRACT

Interactions within galaxy groups are fundamental drivers of galactic evolution, and establishing a direct observational link between the dynamical processes of satellite galaxies and the rejuvenation of massive host galaxies remains challenging. We present a multi-wavelength work of J1611+4026, a unique triple system characterised by a massive early-type host galaxy, Component C and two gas-rich companions, Components A and B, which are currently undergoing a major merger in its near environment. Utilising deep optical imaging from DESI-LS and spectroscopic data from DESI and P200, we employ 2D morphological decomposition using GALIGHT alongside joint spectrophotometric synthesis modelling with BAGPIPES and CIGALE to deconstruct the structural properties and star formation histories of the member galaxies. Crucially, we identify an asymmetric tidal tail extending ~ 15.15 kpc from Component A, confirming the ongoing interaction between the companions. Although Component C appears quiescent in both morphology and spectroscopy, we reveal a subtle robust signal of “minor rejuvenation”, characterised by significant internal dust extinction of $E(B - V) \sim 0.53$ and a UV excess. The reconstructed star formation history indicates a recent (~ 100 Myr) starburst that contributes a negligible fraction to the total stellar mass ($f_{\text{burst}} < 0.1$ per cent). We propose that this activity is fueled by the accretion of metal-enriched gas stripped from the interacting companions. These results strongly suggest group pre-processing, where interactions between satellite galaxies drive low-level star formation in the massive host through gas transfer, providing a quantitative benchmark for interaction-driven evolution in dense environments.

Key words. Rejuvenation – Major Merger – Tidal Stripping – Group Environment – Galaxy Evolution

1. Introduction

Galaxy mergers represent a fundamental mechanism that drives the hierarchical assembly and evolution of cosmic structures. As originally established by Toomre & Toomre (1972), gravitational interactions between galaxies can substantially reshape their morphologies. Specifically, gravitational torques induced during these events drive rapid gas inflows towards galactic centres; this funnelling of cold gas not only triggers intense central starbursts but also fuels active galactic nuclei (AGN; Sanders et al. 1988; Barnes & Hernquist 1996; Hopkins et al. 2006). Empirical studies consistently report that interacting or merging galaxies exhibit star formation rates (SFR) enhanced by a factor of 1.5–4 relative to isolated systems, an effect that notably persists even at projected separations of tens to hundreds of kiloparsecs (kpc; Ellison et al. 2008; Scudder et al. 2012; Patton et al. 2013; Larson et al. 2016). Manifesting physically as diffuse gas “gas bridges” and extended “tidal tails”. These gravitationally induced disturbances redistribute the angular mo-

mentum and constitute direct, observable evidence of the complex gas exchange fueling merger-driven evolution (Toomre & Toomre 1972; Duc & Renaud 2013). While major mergers have been extensively studied as primary triggers for intense starbursts and AGN activity (Sanders et al. 1990; Hopkins et al. 2006), the influence of the galaxy group environment on galaxy evolution is profound. It is within these group environments that galaxies often undergo significant physical transformations before their eventual infall into massive clusters, a phenomenon termed “pre-processing” (Fujita 2004). In particular, interactions between satellite galaxies, as well as those between satellites and the host, constitute complex dynamical processes (Besla et al. 2012; Stierwalt et al. 2015). These mechanisms are capable of stripping gas and redistributing angular momentum, thereby potentially altering the evolutionary trajectory of the entire system (Toomre & Toomre 1972; Barnes & Hernquist 1996).

Massive early-type galaxies (ETGs) are described as “red and dead”, dominated by evolved stellar populations and largely devoid of significant cold gas reservoirs required for star formation (Renzini 2006). However, this conventional paradigm has been challenged by the advent of deep ultraviolet (UV) surveys,

* E-mail: ayuyaosong@gmail.com

** E-mail: jianhui.lian@ynu.edu.cn

which are uniquely sensitive to trace amounts of recent star formation. Indeed, growing empirical evidence indicates that a non-negligible fraction of ETGs exhibit unambiguous signatures of recent star formation activity (Yi et al. 2005; Kaviraj et al. 2007; Davis et al. 2019; Werle et al. 2020; Salvador-Rusiñol et al. 2020; Pandey et al. 2024). One explanation for this phenomenon is the ‘rejuvenation’ scenario, which suggests that originally quiescent galaxies can reignite star formation through the accretion of external gas (Chauke et al. 2019; Wang et al. 2025). Within dense environments, the primary driver of such episodes is often identified as external gas accretion, facilitated either by minor mergers or tidal stripping from gas-rich companions (Davis et al. 2011; Kaviraj 2014). Despite this theoretical framework, establishing a direct observational link between specific interaction events and the onset of rejuvenation in massive host galaxies remains challenging, particularly amidst the complex dynamics of cluster environments (Lotz et al. 2011).

The Milky Way (MW) system offers a local example of satellite–host interaction, currently dominated by the infall of the Large and Small Magellanic Clouds (LMC/SMC) (Besla et al. 2007; Kallivayalil et al. 2013). Crucially, the LMC and SMC are undergoing a strong interaction, generating a massive structure of stripped gas known as the Magellanic Stream (Besla et al. 2012). While the MW provides resolved kinematic details as a local laboratory, our global understanding is intrinsically constrained by an “inside-out” observational perspective. Our position within the Galactic disc complicates the assessment of global properties, as severe dust extinction along the line of sight and distance ambiguities make it difficult to spatially disentangle accreting gas structures from the host galaxy itself (Rix & Bovy 2013; Bland-Hawthorn & Gerhard 2016). Consequently, to comprehensively assess the global impact of such interactions, specifically the mechanisms by which gas stripped from interacting satellites (akin to the LMC–SMC pair) settles onto and rejuvenates massive hosts (Fox et al. 2014). It is imperative to identify extragalactic analogues that offer an unobstructed “outside-in” observational perspective.

We present a detailed multi-wavelength work of J1611+4026 ($z \sim 0.140$), an extragalactic analogue to the MW–LMC–SMC system, combining morphological decomposition via GALIGHT and SED modelling with CIGALE and BAGPIPES to quantify the efficiency of host rejuvenation triggered by gas stripping from its interacting satellites. The paper is organised as follows: Section 2 outlines the discovery and multi-wavelength characterisation of the J1611+4026 system, utilising spectroscopy, photometry, and SED to constrain its physical parameters. Section 3 presents our primary results and quantifies the structural properties of the tidal tail, specifically its projected length and stellar mass. Section 4 discusses the robustness of the adopted models and other possibilities of rejuvenation. Section 5 summarises the main conclusions. Throughout this work, we assume a flat Lambda cold dark matter (Λ CDM) cosmological model with $H_0 = 72 \text{ km s}^{-1} \text{ Mpc}^{-1}$, matter density $\Omega_M = 0.3$, and cosmological constant $\Omega_\Lambda = 0.7$.

2. Data and Method

This section details the discovery and observation of the J1611+4026 system. We characterised the physical and spatial properties of the three member galaxies by combining spectroscopic analysis, photometry analysis, and SED modelling.

2.1. Target Selection

The J1611+4026 system was serendipitously noticed during the compilation of the MGQPC catalog (Chen et al. 2025). The MGQPC catalog is a quasar pair candidate catalog obtained by cross matching version 8.0 of the Million Quasar Catalog (MQC, Flesch 2023) with *Gaia* DR3 (Gaia Collaboration et al. 2023). Before the building of the MGQPC, the MQC version 7.9 was used to cross match with *Gaia* DR3 for pilot testing. The J1611+4026 system initially consists of J1611+4026A and B, where A comes from the MQC version 7.9 as an AGN candidate, while B comes from *Gaia* DR3 as a candidate for a quasar pair member. This system seems like an AGN pair with both host galaxies relatively obvious, and might be mutually interacting with each other. Therefore, we took a spectroscopic follow-up for this system.

2.2. Spectroscopy

Long-slit spectroscopic follow-up was carried out for J1611+4026A and B using the Dual Spectrograph (DBSP) equipped on the 200-inch Hale Telescope (P200) at Palomar Observatory, California, on the night of 5th Sep. 2024 (P.I. Zizhao He). The dichroic D-55 was used to obtain the spectra at the blue and red arms. The exposure time for both sources and both arms is 900 seconds. The 300 lines/mm grating blazed at 3990 Å was chosen for the blue arm, while the 316 lines/mm grating blazed at 7150 Å for the red arm. This provides a dispersion of 2.108 Å/pixel and 1.535 Å/pixel for the blue and red arms (Oke & Gunn 1982). The seeing during the exposure of this system was $\sim 1.7''$, and a $1.5''$ -wide slit was chosen. In the spectrum of the red arm, there is a bad CCD region at the wavelength of ~ 5800 – 6250 Å, thus the spectra of both sources are unavailable in this range.

J1611+4026A, J1611+4026B, and J1611+4026C; hereafter referred to as A, B, and C, respectively. Components A and B were selected from MQC. A visual inspection of the DESI footprint around Component A galaxy environment revealed a third companion, Component C, with a concordant redshift of $z = 0.1403$. Figure 1 presents the pseudo-colour image of the J1611+4026 system. The spectroscopic redshifts confirm the physical association of the triplet. Notably, a faint tidal tail extends from Component A, which is highlighted by blue arrows. It is indicative of ongoing gravitational interaction. The consistent redshifts across Components A, B, and C indicate that they form a physically associated system rather than an accidental projection. Based on their angular coordinates, we derived a projected separation of only 9.038 kpc between Components A and B, and 46.352 kpc between Component A and Component C. Projected separations of < 30 kpc are generally considered a strong indicator of an ongoing merger, placing the system well within the regime of strong gravitational interaction (Ellison et al. 2010). Furthermore, previous studies establish 150 kpc as a reliable upper limit for interaction-induced star formation (e.g. Patton et al. 2013), suggesting that the entire ABC system is dynamically active. Consequently, we propose that A and B are currently merging and will likely be subsequently accreted by the massive host, Component C, to form a massive galaxy. However, verifying these dynamical hypotheses requires precise radial velocity constraints, which we address in detail in Section 4.3.

Both the SDSS and DESI surveys had observed component C; upon evaluating the survey depth and signal-to-noise ratio (S/N), we selected the superior DESI spectra to charac-

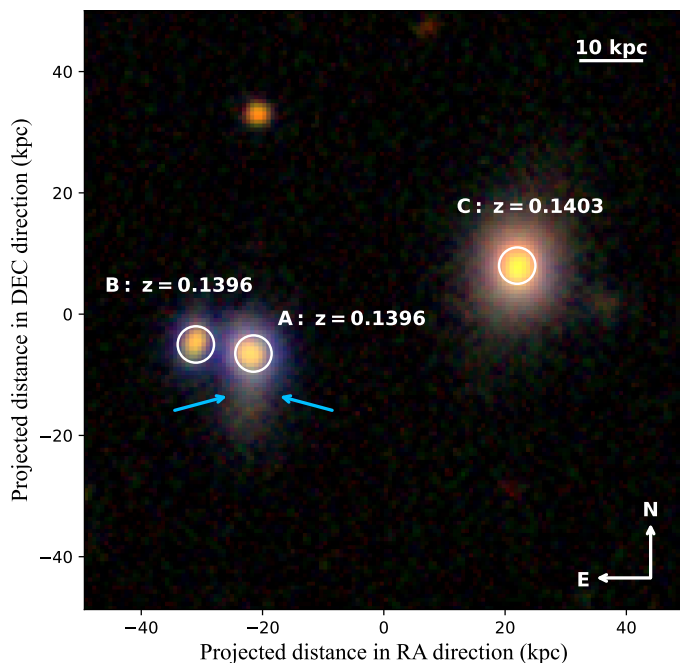


Fig. 1. Pseudo-color image of the J1611+4026 system covering a $40'' \times 40''$ field of view. The blue arrows highlight the tidal tail of J1611+4026A. The white circles indicate the apertures used for photometry.

Table 1. Basic features of J1611+4026 system.

Name ⁽¹⁾	R.A. ⁽²⁾ (deg)	Dec ⁽³⁾ (deg)	<i>r</i> -band ⁽⁴⁾ (mag)	redshift ⁽⁵⁾
J1611+4026A	242.9772	40.4359	18.16	0.1396
J1611+4026B	242.9785	40.4362	19.58	0.1396
J1611+4026C	242.9707	40.4375	17.36	0.1403

Notes. Columns (2) and (3) are J2000 coordinates.

terise Component C as shown in the lower panel of Figure 2. Spectral fitting was performed using QSOFITMORE, an advanced Python module derived from QSOFIT (Fu 2021) and optimised for analysing quasar and galaxy spectra. Widely adopted in recent studies, the utility and reliability of this code have been extensively demonstrated (e.g. Fu et al. 2022; Pang et al. 2025; Liang et al. 2025, see Appendix A for detailed spectral fitting).

Table 1 lists the basic properties of the J1611+4026 system, including coordinates, DESI *r*-band magnitudes, and spectroscopic redshifts. The spectrum and spectroscopic redshift z_{spec} of Component C were retrieved from DESI-DR1¹ (DESI Collaboration et al. 2025) using the Spectra Analysis and Retrieval Catalog Lab (SPARCL) from the Astro Data Lab². The spectral landscape of Component C differs markedly, showing an absence of nebular emission consistent with “lineless” retired galaxies, where deep stellar absorption troughs likely overwhelm weak intrinsic activity (Herpich et al. 2018). Consequently, spectroscopic indicators are deemed unreliable for this Component, and we instead rely on the SFR inferred from broadband SED fitting using CIGALE.

2.3. Photometry and Morphology

We identified the three components of the system (A, B, and C) using photometric data. For this analysis, we utilised deep optical imaging retrieved from the DESI Legacy Imaging Surveys (DESI-LS; Dey et al. 2019). Integrating data from the DECaLS, MzLS, and BASS surveys, DESI-LS offers the high sensitivity and uniform calibration essential for reliable source characterisation. While the survey typically provides coverage in *g*, *r*, *i*, *z*, we noted that *i*-band data were unavailable for our Component. Consequently, we employed the *g*, *r*, and *z* bands for photometric measurements, selecting the *g*-band for structural decomposition due to its superior seeing conditions.

To quantify the structural properties and surface brightness profiles of our Components, we employed the Python-based package GALIGHT³ (Ding et al. 2020). Built upon the modelling engine LENSTRONOMY (Birrer et al. 2021), GALIGHT provides an automated framework for identifying source components, estimating background noise, and constructing Point Spread Functions (PSFs). Its capability to robustly disentangle complex light distributions, particularly in systems containing AGN or merger features. It has been extensively validated in large-scale studies (e.g. Ding et al. 2023). Moreover, recent applications to complex interacting systems, such as 3C 59 (Wang et al. 2025), demonstrate its efficacy in recovering clean residual images. Given these attributes, GALIGHT was uniquely suited for separating the diffuse flux of tidal features from the host galaxies in the J1611+4026 system.

We performed a 2D surface brightness decomposition using GALIGHT. Modelling results derived from the DESI *g*-band imaging are presented in Figure 3. As illustrated in the upper panel, best-fit models for the interacting pair (Components A and B) successfully reproduce the observed light distributions, yielding minimal residuals in the central regions. Normalised residual maps indicate that the primary structural components are well-described by single Sérsic profiles. However, faint asymmetric residuals persist in the periphery, indicative of tidal perturbations. Similarly, the isolated Component C is accurately modelled by a smooth Sérsic profile as shown in lower panel, exhibiting no significant substructure.

2.4. SED Analysis

To derive the physical properties of the three Component galaxies, we employed the Python-based SED fitting code CIGALE (Code Investigating GALaxy Emission, Boquien et al. 2019; Noll et al. 2009). The photometric baseline comprised optical data from the Pan-STARRS survey (Chambers et al. 2016) and infrared constraints from the WISE W1 and W2 bands (Wright et al. 2010). For Component C, this dataset was augmented by ancillary high-resolution coverage, including ultraviolet photometry from GALEX NUV (Martin et al. 2005) and near-infrared (*J*, *H*, *K_s*) observations from 2MASS (Skrutskie et al. 2006). Conversely, for components A and B, we treated the WISE photometric measurements as upper limits (indicated by green inverted triangles in Figure 4). This conservative strategy was necessitated by the small projected separation between the pair (~ 9 kpc), which is approaching the instrument’s resolution limit. Although we utilised resolution-enhanced unWISE coadds (Lang 2014; Schlafly et al. 2019) to mitigate source blending, we imposed upper limits on these constraints to ensure the robustness of the derived physical parameters.

¹ <https://data.desi.lbl.gov/doc/>

² <https://datalab.noirlab.edu/index.php>

³ <https://github.com/dartoon/galight>

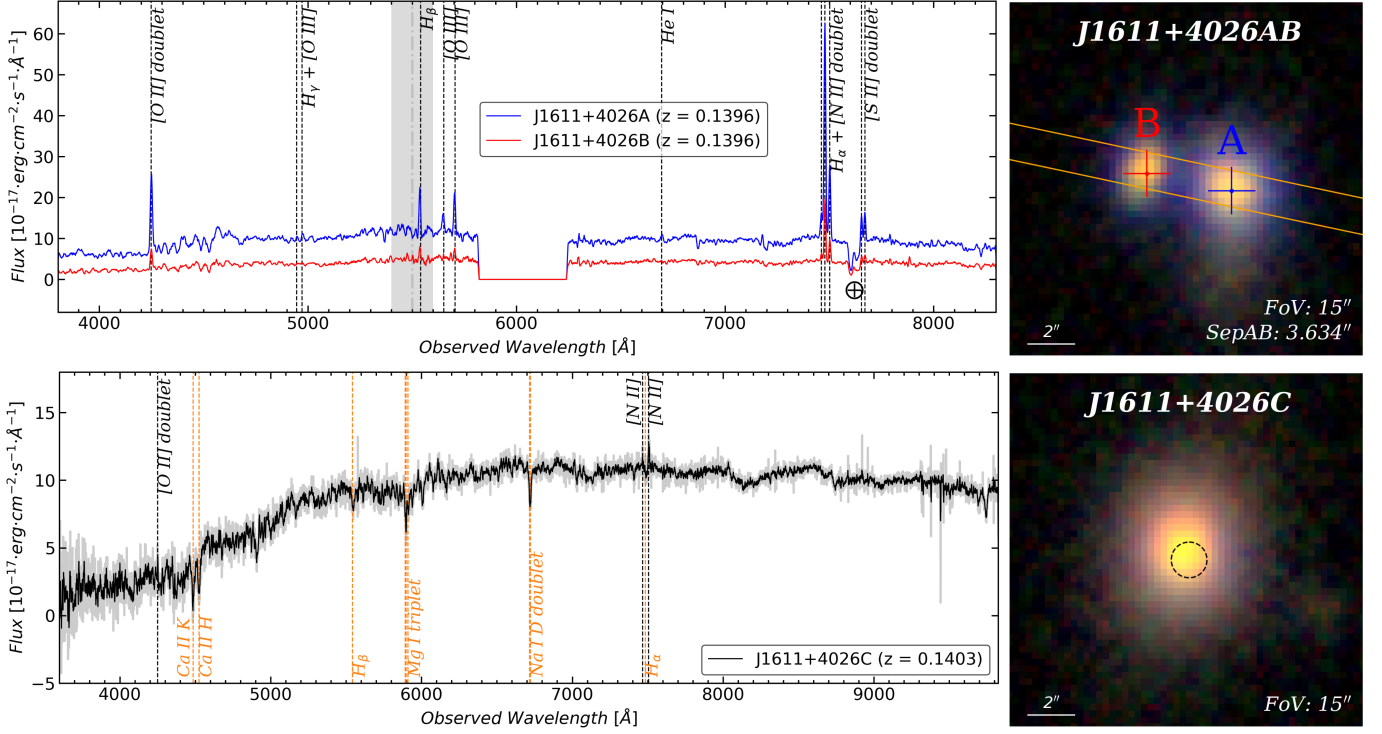


Fig. 2. Upper panel: DBSP/P200 spectra of Component A and B (left), and their pseudo-colour cutout image with observation slit (orange) overlapping on it (right). The black overlapping region denotes the stitching of the blue and red spectral bands, while the crossed circles indicate telluric absorption. Lower panel: DESI-DR1 spectrum of Component C, with its pseudo-colour image shown on the right.

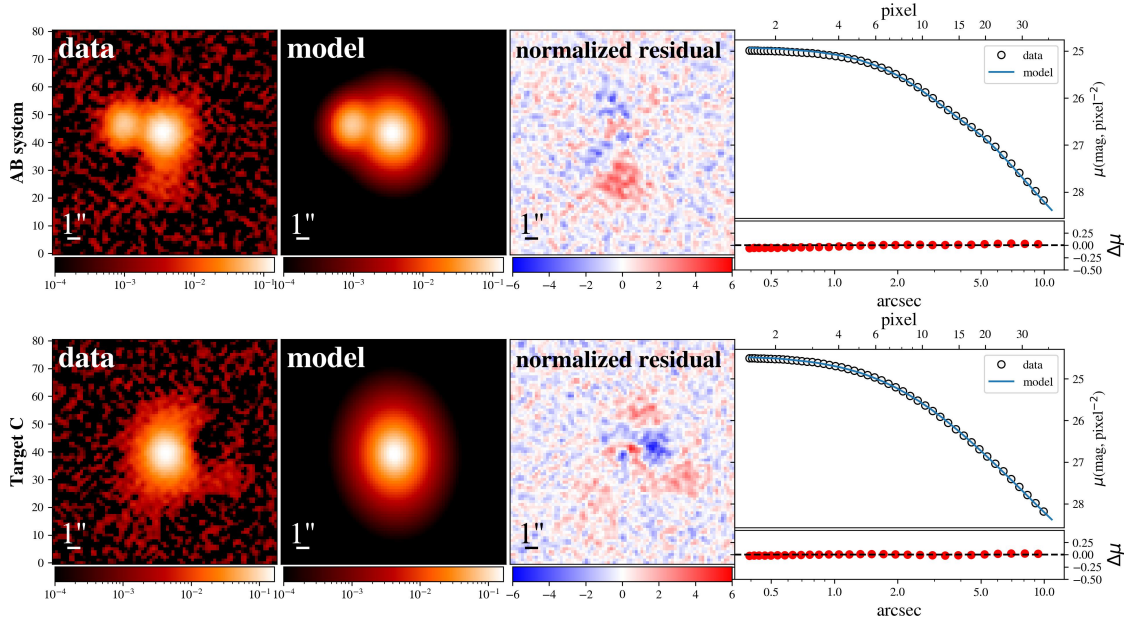


Fig. 3. 2D decomposition of J1611+4026 system and the surrounding galaxies for the DESI g-band images with GALIGHT. For each panel, from top to bottom, represents Component A, Component B, and Component C. From left to right, represents data, model, data minus model (residual), and their surface brightness profile. The defect in the Component C data panel is intrinsic to the DESI-LS observational data; this region was masked during the fitting process to prevent any bias in the derived structural parameters.

Best-fit SED models are presented in Figure 4. These models reproduce observed fluxes across all available passbands for the three Components. The associated reduced chi-squared values (χ_r^2) indicate statistically reliable solutions. As evidenced by the residual panels, deviations between model and observed fluxes

are minimal; this confirms the robustness of the adopted stellar population synthesis models and dust attenuation prescriptions. Given the interacting nature of the J1611+4026 system, we incorporated the Stalevski et al. (2016) model into our SED fitting, allowing the AGN fraction to vary freely to account for

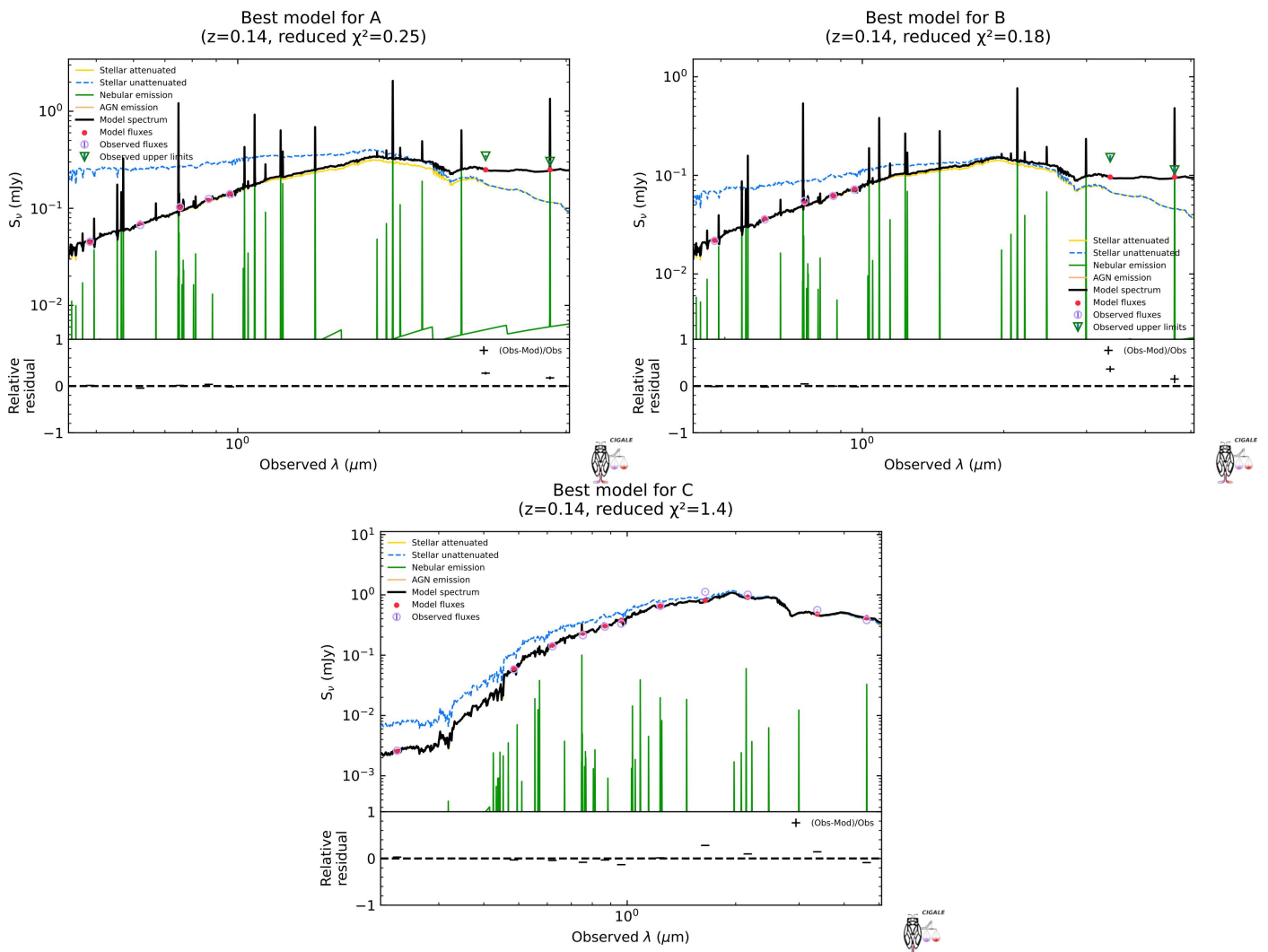


Fig. 4. Best-fit SEDs for Components A, B, and C modelled with CIGALE. The details of the observational data fitting are introduced in Section 2.4, and the results are shown in Table 3. The details about the input parameters are shown in Table C1.

potential mid-infrared contamination from hot dust. The fitting yielded negligible AGN contributions for all members, with derived f_{AGN} values of 0.075, 0.042, and 0.018 for Components A, B, and C, respectively. These low fractions validate the robustness of our stellar mass and SFR estimates, implying that the infrared emission of the system is driven primarily by star formation. Full parameters derived from the SED fitting are detailed in Appendix 3.

3. Result

We present a comprehensive analysis of the J1611+4026 system. We begin by characterising the physical properties of the individual components based on spectroscopic, photometric and SED result. Subsequently, we detail the morphological identification of the tidal features and conclude with an assessment of Component C evolutionary history.

3.1. General Properties of System

Quantitative structural parameters derived from the g , r , and z bands are summarised in Table 2. In all cases, reduced chi-square

values (χ^2_{ν}) approximate unity, confirming the robustness of the fits. For Component A, we measured effective radii (R_e) ranging from 0.47 to 0.87 kpc and Sérsic indices (n) varying from 0.91 (g -band) to 4.57 (z -band). The steep increase in n at longer wavelengths implies that Component A possesses a compact, bulge-dominated core, most pronounced in the near-infrared, while a more extended disc component dominates the blue optical emission. In contrast, the companion Component B exhibits consistently smaller effective radii ($R_e \sim 0.2\text{--}0.6$ kpc) and lower Sérsic indices ($n \sim 0.4\text{--}1.8$), consistent with a low-mass, disc-dominated satellite. We note that the z -band emission of Component B appears diffuse with a relatively low S/N. Allowing n to vary freely in this band resulted in parameter degeneracy and unstable convergence. Therefore, to ensure physical robustness, we fixed the index to $n = 1.0$ (consistent with an exponential disc), yielding stable residuals. Morphologically, Component C displays characteristics typical of a lenticular (S0) galaxy.

The main physical parameters derived from our spectral analysis are presented in Table 3. Due to different S/N of spectra, we adopted a hierarchical approach to estimate SFRs, tailoring the methodology to the specific constraints of each source. For Component A, which exhibits robust nebular lines, SFRs were determined directly from the $H\alpha$ luminosity, corrected for

Table 2: Best-fit Structure Properties for AB system and Component C with GALIGHT

Table 2. *

Parameter	Symbol	Component A	Component B	Component C
<i>g</i> band				
Effective radius	$R_{e,g}$ (kpc)	0.87 ± 0.01	0.63 ± 0.01	1.05 ± 0.01
Sérsic index	$n_{\text{sérsic},g}$	0.91 ± 0.02	0.44 ± 0.03	1.08 ± 0.02
Reduced χ^2	χ_r^2	0.99	0.99	1.02
<i>r</i> band				
Effective radius	$R_{e,r}$ (kpc)	0.60 ± 0.01	0.21 ± 0.03	0.94 ± 0.01
Sérsic index	$n_{\text{sérsic},r}$	3.21 ± 0.10	1.76 ± 0.35	1.66 ± 0.05
Reduced χ^2	χ_r^2	1.23	1.23	0.88
<i>z</i> band				
Effective radius	$R_{e,z}$ (kpc)	0.47 ± 0.01	0.16 ± 0.02	0.97 ± 0.01
Sérsic index	$n_{\text{sérsic},z}$	4.57 ± 0.24	1.00 ± 0.00^a	1.61 ± 0.07
Reduced χ^2	χ_r^2	0.99	0.99	1.03

Note.

^a The Sérsic index of Component B z band is fixed to 1.0 during the image decomposition (see details in Section 4.1).

dust attenuation via the Balmer decrement (assuming an intrinsic Case B ratio of 2.86 and a Calzetti et al. (2000) law). These calculations adhere to the standard Kennicutt (1998) calibration, scaled to a Salpeter Initial Mass Function (IMF). Conversely, the H β flux in Component B is compromised by low S/N, resulting in an unphysical Balmer decrement (< 2.86). To maintain rigour, we therefore report the uncorrected $SFR_{H\alpha}$ as a strict lower limit.

Derived physical parameters are summarised in Table 3, alongside emission line measurements obtained via QSOFITMORE (as detailed in Section 2.2). We identified Component A as the primary star-forming component of the interacting pair, characterised by a stellar mass of $M_\star = (1.46 \pm 0.25) \times 10^{10} M_\odot$ and significant internal dust extinction $E(B - V)_{\text{SED}} = 0.54 \pm 0.16$. Notably, the SFR derived from SED fitting aligns with the instantaneous rate estimated from H α emission ($SFR_{H\alpha} \approx 3.53 M_\odot \text{yr}^{-1}$), corroborating the picture of active, ongoing star formation. While the companion Component B is less massive ($M_\star \approx 0.75 \times 10^{10} M_\odot$), it retains non-negligible activity ($SFR_{H\alpha} \approx 0.57 M_\odot \text{yr}^{-1}$). In stark contrast, the massive host (Component C; $M_\star \approx 5.37 \times 10^{10} M_\odot$) exhibits a negligible star formation rate ($SFR_{H\alpha} \approx 0.07 M_\odot \text{yr}^{-1}$), consistent with the profile of a quiescent early-type galaxy.

Despite the spectroscopic classification of Component C as a massive quiescent galaxy, SED fitting revealed a notably high dust attenuation $E(B - V)_{\text{SED}} = 0.53 \pm 0.15$. This value deviates markedly from the typical dust content of local massive ETGs, which generally exhibit negligible extinction (Rowlands et al. 2012). Such an excess suggests the presence of a substantial reservoir of diffuse interstellar medium (ISM) obscured within the galaxy; while potentially accreted from the environment, this material likely lacks the surface brightness required to manifest as visible tidal features in our current imaging. This discrepancy necessitates a deeper investigation into the evolutionary history of the system. Therefore, in Section 3.2, we reconstruct the Star Formation History (SFH) of Component C to probe for recent accretion events or suppressed star formation.

3.2. Evolutionary history

As illustrated in panel (a) of Figure 5, Component A resides on the Star-Forming Main Sequence (SFMS) at $z \sim 0.14$, while Component B is presented as a strict lower limit due to low S/N in the H β line (e.g. Popesso et al. 2023). Accounting for the estimated extinction moves Component B upwards, indicating that both satellite galaxies maintain active star formation commensurate with their stellar masses and implying the presence of substantial gas reservoirs. The evolutionary status of these galaxies is further substantiated by the Mass-Metallicity Relation (MZR) presented in panel (b). While Component A lies a bit below the local reference relation (Lian et al. 2018), Component B is located marginally above the trend given its lower stellar mass. Notably, despite the difference in stellar mass, the gas-phase oxygen abundances defined as $12 + \log(\text{O}/\text{H})$ are consistent between the two galaxies (~ 8.65 – 8.67). This marginal offset in Component A aligns with the prominent tidal features, suggesting potential metallicity dilution driven by interaction-induced inflows of metal-poor gas (e.g. Ellison et al. 2008), while the chemical homogeneity across the pair strongly implies that the accreting gas is effectively mixed or transferred between the neighbouring systems rather than being pristine material from the intergalactic medium. Panel (c) displays the distribution of the AB system in the rest-frame UVJ diagram; both satellites occupy the blue star-forming region, situated well outside the passive wedge defined by Schreiber et al. (2015). Collectively, these diagnostics confirm that Components A and B are gas-rich donors capable of fuelling the observed interaction.

In stark contrast to the active AB pair, Component C exhibits characteristics typical of a massive, quenched galaxy while displaying subtle signatures of recent activity. As depicted in panel a of Figure 5, Component C lies significantly below the SFMS, exhibiting a specific star formation rate (sSFR) nearly 1.5 dex lower than the trend line. Concurrently, panel c places the galaxy within the region typically populated by red-sequence systems dominated by evolved stellar populations (Schreiber et al. 2015). These global metrics indicate that the bulk of stellar mass in

Table 3. Summary of Main Emission Lines for Three Spectrum-Defined Galaxies

Name	H α	$SFR_{H\alpha}$	SFR_{SED}	$M_{\star,SED}$ ($10^{10} M_{\odot}$)	$E(B - V)_{SED}$	Metallicity (N_2)
A	499.6 ± 10.60	6.37 ± 1.10	< 3.28	1.46 ± 0.25	0.54 ± 0.16	8.66 ± 0.006
B	134.7 ± 3.31	0.59 ± 0.015	< 1.85	0.75 ± 0.16	0.45 ± 0.18	8.67 ± 0.012
C	-	-	0.58	5.37 ± 1.40	0.53 ± 0.15	-

Note. For Component C, the low S/N of the spectrum precluded a robust fit to the H α emission line. We were unable to derive an accurate $SFR_{H\alpha}$ and metallicity.

Component C formed in the distant past, implying the galaxy has undergone effective quenching. However, the detailed Star Formation History reconstruction presented in panel d reveals a more complex narrative. Derived from a joint analysis of spectroscopy and photometry using BAGPIPES (Carnall et al. 2018), the SFH exhibits a bimodal distribution. The fitting parameters of BAGPIPES are shown in Table 4. The vast majority of stellar mass formed at $z > 1$, followed by a prolonged quiescent epoch lasting approximately 6 Gyr, as evidenced by near-zero star formation rates at intermediate ages. Crucially, the inset highlights a sharp, recent burst of star formation occurring within the last ~ 100 Myr. Although this late-time activity contributes a negligible fraction to the total stellar mass, where $f_{\text{burst}} < 0.1$ per cent, it is essential within the model to reproduce the observed UV excess and nebular emission lines discussed previously. Combining global quenching morphology with a temporally distinct, recent starburst aligns with a “minor rejuvenation” scenario (Chauke et al. 2019). The extended quiescent gap rules out continuous secular evolution, strongly implying that the recent activity was externally triggered. The most probable source is the accretion of tidal gas stripped from the interacting neighbours, specifically the AB system. A more detailed analysis is presented in Section 4.1.

3.3. Identification of Tidal Tail

Identifying faint tidal features is critical for confirming the merger origin of the system. Upon modelling and subtracting the light distributions of Components A and B via the 2D decomposition code GALIGHT as shown in Figure 3 upper panel. We detected a coherent, low-surface-brightness structure in the residual map. Extending outward from the primary galaxy (Component A), this feature exhibits significant asymmetry. To quantify the stellar mass contained within this tidal debris, we performed aperture photometry on the normalised residual map. As illustrated in Figure 6, we defined a wedge-shaped aperture to encompass the full azimuthal and radial extent of the emission while minimising contamination from background sky noise. We derived the stellar mass of the tidal tail by converting its integrated luminosity. Assuming the tidal tail consists of stellar populations stripped from the outskirts of the primary progenitor, we adopted the mass-to-light ratio (M/L) of Component A for the debris. We calculated the g -band M/L ratio (Y_g) using the total stellar mass derived from SED fitting (see Section 2.3) combined with the intrinsic DESI-LS g -band luminosity. Applying this Y_g to the residual flux measured within the aperture yielded a stellar mass of $6.03 \times 10^8 M_{\odot}$. This value represents a lower limit, as diffuse tidal material may remain below the detection threshold of the imaging data.

To further constrain the spatial scale of the tidal tail, we analysed the one-dimensional surface brightness profile along the ex-

tended tail. We positioned a pseudo-slit across the system, indicated by the red rectangle in the left panel of Figure 7. The slit was oriented to trace the maximum extension of the tidal feature. Crucially, we centred the slit on the photometric core of Component A, ensuring it strictly avoided light contamination from the companion, Component B. This configuration facilitated a direct comparison between the upper section, representing the unperturbed stellar profile of the host. The lower section contains the merger-induced excess. The extracted surface brightness profile is displayed in the right panel of Figure 7. The data revealed a distinct dichotomy: while the main galaxy light followed the steep decline typical of the host, the tidal tail exhibited a significant surface brightness excess at radii $R \gtrsim 8$ pixels. To quantify this structure, we modelled the profiles on both sides using exponential functions. The unperturbed side of the host was accurately fitted by a single exponential profile with a scale length of $h \approx 2.94$ pixels. In contrast, the tail side necessitated a double-exponential model to simultaneously describe the core and the extended excess. Fitting results indicated that the tidal debris possessed a significantly extended scale length of $h_{\text{tidal}} \approx 23.73$ pixels, corresponding to ~ 15.15 kpc. This extended scale length is consistent with the characteristics of dynamically cold debris formed via gravitational interactions.

4. Discussion

In this section, we discuss the physical interpretation of the J1611+4026 system. We investigate the evidence for the rejuvenation of Component C and assess the robustness of this signal. Drawing a comparison with the MW-LMC-SMC analogue, before critically evaluating alternative scenarios, including AGN activity, the UV upturn, and environmental effects.

4.1. Rejuvenation of Component C

The substantial dust extinction derived from the SED fitting $E(B - V)_{SED} \sim 0.53$ presents a paradox: while Component C exhibits the optical spectroscopy and morphology of a passive disk galaxy (S0 galaxy), it appears to harbour a significant reservoir of ISM typically associated with active star formation. To resolve this tension and dissect the composite stellar populations, we performed independent fits on both the 11-band photometry and the DESI optical spectrum of Component C employing the Bayesian analysis code BAGPIPES (Carnall et al. 2018). Table 4 details the fitting parameters utilised in BAGPIPES. Unlike broad-band photometry, which suffers from severe age-metallicity degeneracy. Full spectral fitting enables the disentanglement of multiple stellar components by simultaneously constraining nebular emission lines and age-sensitive stellar absorption features, such as the 4000 Å break and Balmer absorption series (Conroy 2013; Carnall et al. 2019). Consequently,

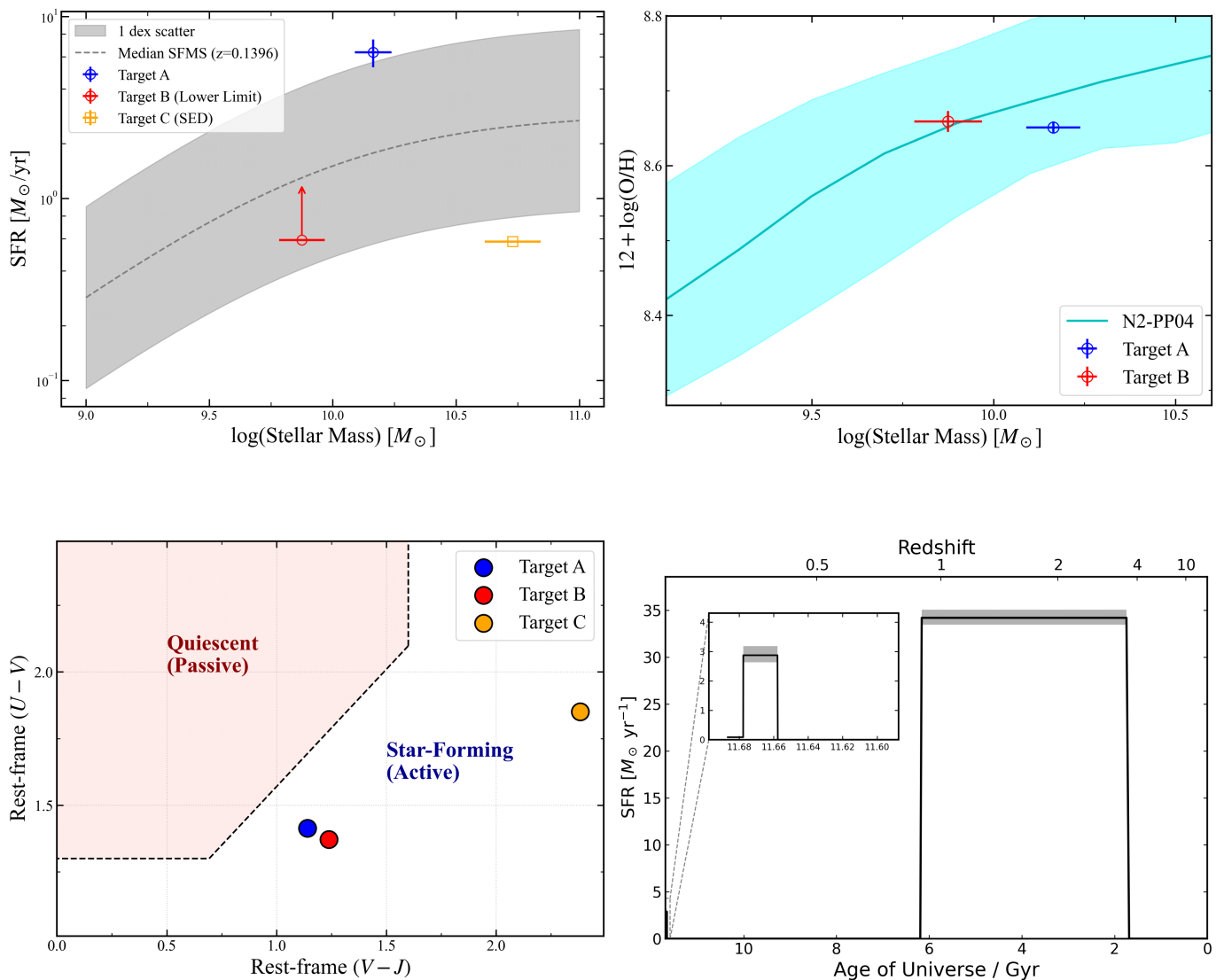


Fig. 5. Physical properties and evolutionary status of the Component A, B, and C system. Panel (a): The position of the Components on the SFMS at $z \sim 0.14$ from Popesso et al. (2023). The dashed line and grey shaded region represent the median relation and ± 0.5 dex scatter. The red upward arrow indicates the lower limit for Component B, while the square denotes the SFR derived from SED fitting for Component C. Panel (b): Relationship between stellar mass and metallicity. The trend line is from Lian et al. (2018). Panel (c): Rest-frame UVJ diagram. Rest-frame U, V, and J magnitudes are estimated from the best-fit broadband SED (see Section 2.4). The solid lines delineate the boundaries of the quiescent (top left) and star-forming (bottom) populations, as defined by Schreiber et al. (2015). Component C resides near the quiescent wedge, consistent with its red colours, while Components A and B occupy the star-forming region. Panel (d): The reconstructed SFH of Component C derived from BAGPIPES (Carnall et al. 2018). The main plot shows the posterior distribution of the SFR over cosmic time, whilst the inset highlights the recent epoch, revealing potential signatures of rejuvenation or low-level activity.

we adopted the results derived from the spectroscopic data, as they provided tighter constraints on the evolutionary history. The reconstructed SFH is presented in the panel (d) of Figure 5.

Figure 5 reveals a distinct bimodal evolutionary path. The galaxy formed the vast majority of its stellar mass during a primordial epoch at high redshift ($z > 1.5$, corresponding to a cosmic age of $\sim 2 - 4$ Gyr). This intense phase of early mass assembly is characteristic of the “downsizing” scenario, in which the most massive galaxies form their stars rapidly in the early Universe before quenching (Neustein et al. 2006). Following this major burst, Component C appears to have undergone a prolonged period of passive evolution spanning several gigayears, consistent with its red, early-type appearance in optical imaging.

However, panel (d) of Figure 5 reveals a secondary, recent episode of star formation, a rejuvenation event, occurring at the observed redshift $z \sim 0.14$. We detect an instantaneous SFR of $\sim 3 M_{\odot} \text{yr}^{-1}$ during this epoch. Although this young population contributes a negligible fraction < 1 per cent to the total stellar mass, its presence confirms that Component C is not a “red and dead” fossil. Instead, the galaxy is well-described by the “frosting” model (Trager et al. 2000), in which a veneer of young stellar population is superimposed onto an old, massive bulge. This recent rejuvenation provides a natural explanation for the high dust content inferred from SED analysis. This suggests that Component C has recently accreted cold, metal-enriched gas, likely stripped from the interacting companions, Components A and B, or acquired via minor mergers, which is currently cool-

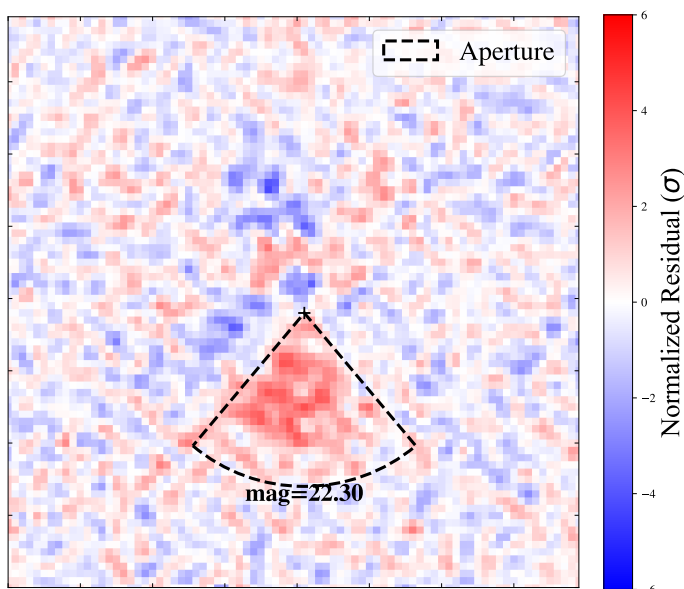


Fig. 6. Normalized residual map (in units of σ) of the g -band image. The black dashed wedge indicates the aperture defined to measure the flux of the faint tidal feature, yielding an integrated magnitude of $m_g = 22.30$.

ing and fueling a new generation of stars (Kaviraj et al. 2007; Yi et al. 2005).

We note that enhanced star formation is typically triggered in the early stages of a galaxy encounter, whereas AGN activity tends to peak post-merger (Ellison et al. 2013). This dynamical timeline may explain the absence of prominent tidal tails in the optical imaging of Component C, suggesting the system is in a phase where the gas response precedes significant morphological disruption. Furthermore, we acknowledge the possibility that the interaction involves a fly-by scenario with Components A and C; the implications of this dynamical configuration are discussed in Section 4.3.

4.1.1. Robustness of the Rejuvenation Signal

To assess the robustness of the detected minor rejuvenation signal and mitigate the well-known degeneracy between stellar age and dust attenuation, we performed a detailed posterior analysis using BAGPIPES. Unlike grid-based approaches, the nested sampling algorithm employed by BAGPIPES facilitates a direct visualisation of parameter covariances, to determine whether the inferred young stellar population is merely an artefact arising from overestimated extinction (Carnall et al. 2018).

We explicitly examined the joint posterior distribution of dust attenuation (A_V) and the recent star formation strength (parameterised as $\Delta \log(\text{SFR})_{\text{recent}}$ in the continuity model), as presented in Appendix B. Crucially, confidence contours exhibit a distinct lack of diagonal covariance between these two parameters. As illustrated in the corner plot, dust attenuation is tightly constrained to $A_V = 1.05 \pm 0.04$ mag and remains stable across a wide range of recent star formation solutions, spanning from quiescent to bursty scenarios. This morphology confirms that high dust content is a robust feature driven by the spectrophotometric data, specifically the NUV excess and continuum slope, rather than a model-dependent trade-off with stellar age. Consequently, the inclusion of a minor rejuvenated population is required to

reproduce the SED, even when the dust is independently constrained.

Building upon these robust constraints, we quantified the strength of the recent starburst. The best-fit solution yielded a negligible burst mass fraction, establishing a robust upper limit of $f_{\text{burst}} < 1$ per cent at the 3σ confidence level. We emphasise that despite this negligible mass contribution, the presence of this young population is essential to reproduce the observed NUV excess and nebular emission features, thereby precluding model overfitting.

To further validate this conclusion, we compared our results with the analysis performed using CIGALE. After reconciling the divergent dust definitions employed by the two codes, CIGALE yielded a nebular colour excess of $E(B-V)_{\text{lines}} \approx 0.53$. Adopting the canonical relation for starburst galaxies, where $E(B-V)_{\text{stars}} \approx 0.44 \times E(B-V)_{\text{lines}}$ (Calzetti et al. 2000), and the Calzetti attenuation curve with ($R_V = 4.05$) utilised in CIGALE, we derived a stellar continuum extinction of $A_V \approx 0.94$ mag. This value aligns with the BAGPIPES estimate within 1σ . Such concordance reinforces the conclusion that the substantial extinction in this early-type galaxy is a physical reality independent of the modelling technique. Confirming of such significant extinction accompanied by a trace amount of young stars in an early-type galaxy supports an external origin for the ISM, likely acquired via recent gas-rich interactions rather than through internal evolution.

4.2. The MW-LMC-SMC Analogue

The spatial configuration and projected separations of the Component system bear a striking resemblance to the local triple system comprising MW, the LMC, and the SMC. However, we note a quantitative distinction: the satellite-to-host stellar mass ratio in J1611 ($(M_A + M_B)/M_C \sim 0.4$) is significantly higher than that of the MW-LMC system (~ 0.1). Consequently, J1611+4026 likely represents a scaled-up, more dynamically violent version of the interaction, potentially driving more efficient gas transfer than currently observed in the Local Group. In this morphological analogue, Component C corresponds to the massive central host of the MW, while Component A and Component B mirror the roles of the accreting satellites, the LMC and SMC, respectively. The Magellanic Clouds exhibit a complex history of mutual interaction (e.g. Besla et al. 2007, 2012), and are currently interacting with the Galactic potential; predicted to undergo orbital decay, they will eventually merge with the MW driven by dynamical friction (Cautun et al. 2019). While the morphological similarities are compelling, verifying this dynamical scenario requires precise constraints on radial velocities and orbital trajectories. We present a detailed kinematic analysis and discussion of the system’s 3D geometry in the subsequent section.

Crucially, the J1611+4026 system offers a valuable extragalactic perspective, complementing our internal understanding of the Local Group. Studies of the MW are inevitably limited by “inside-out” observational bias. Our position within the galactic disc complicates assessments of global galactic properties, specifically dust extinction, which hinders efforts to quantify the total budget of accreting gas and the net efficiency of merger-induced star formation (e.g. Rix & Bovy 2013; Bland-Hawthorn & Gerhard 2016). In contrast, the J1611+4026 system provides an unobstructed “outside-in” vantage point. This panoramic view allows us to spatially integrate the entire interaction event, thereby precisely quantifying the direct impact of satellite accretion on the massive host. The negligible burst mass fraction ($f_{\text{burst}} < 0.1\%$) derived for Component C provides

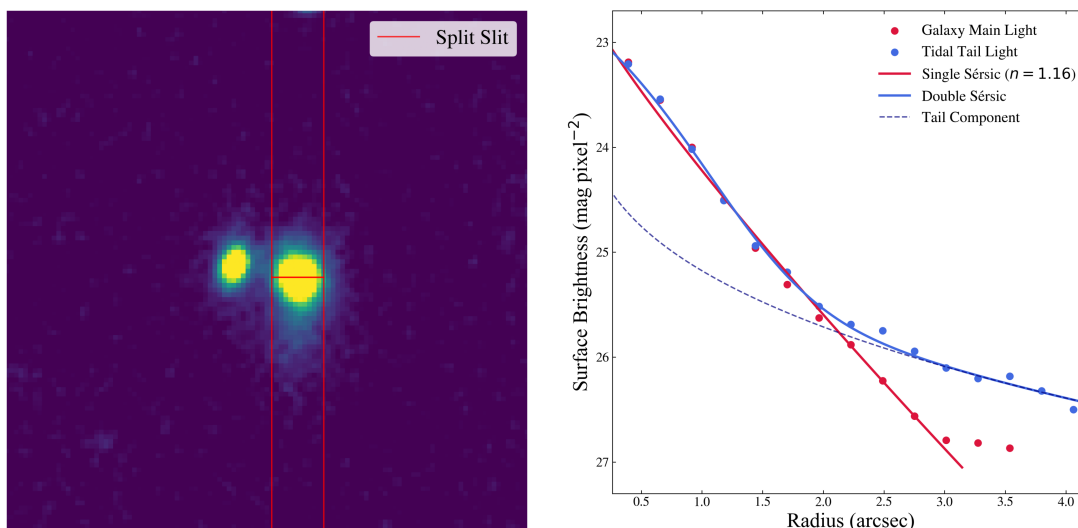


Fig. 7. Left: The g -band image showing the placement of the pseudo-slit (red lines) along the tidal feature. Right: Surface brightness profile extracted from the slit. The main galaxy light (red circles) is well-fitted by a single Sérsic profile ($n = 1.16$; red line). The tidal tail region (blue circles) shows a clear excess at $R > 2.096$ arcsec, which is best described by a double-component model (blue solid line; dashed line represents the isolated tail component).

Table 4. Summary of BAGPIPES Fitting Parameters

Component	Parameter	Configuration / Prior
Physical Parameters		
Star Formation History	Model Type	Continuity (Non-parametric)
	$\log(M_*/M_\odot)$	Uniform: [6.0, 13.0]
	Metallicity (Z)	Log-10: [0.01, 2.5] Z_\odot
	Time Bins	8 bins (0 Myr – 10 Gyr)
Nebular Emission	$\log U$	–3.0
Dust Attenuation	Law	Calzetti
	A_V	Uniform: [0.0, 4.0]
Redshift	z	0.1403

a quantitative benchmark for such interactions. This suggests that while Magellanic encounters are dynamically active, they may induce only minor rejuvenation episodes or localised star formation without driving significant structural perturbations or mass growth in the host (see Naab et al. 2009). Hopkins et al. (2010) demonstrated that minor mergers are less disruptive, primarily contributing to the growth of low B/T systems without destroying the host’s disc-like structure. Identifying a system captured at such a specific evolutionary stage, where satellites are actively interacting while the host exhibits detectable starburst signatures, remains rare in current surveys (e.g. Ellison et al. 2013; Patton et al. 2013). Consequently, this system serves as a unique laboratory for predicting future interactions between the MW and its satellite companions.

4.3. Alternative Scenarios

Having established the presence of a young stellar component in Component C, we rigorously excluded non-star-forming mechanisms capable of mimicking these characteristics. Specifically, we investigated potential contamination from AGN, and contributions from evolved stellar populations responsible for the “UV

upturns”. Finally, we explored the dynamical origin of the cold gas reservoirs fuelling this rejuvenation.

4.3.1. AGN Activity

Investigating whether the emission characteristics and infrared colour originate from black hole accretion, we employed the mid-infrared colour selection criterion based on WISE photometry. While active galaxies with power-law SEDs typically exhibit a red mid-infrared colour arising from hot circum-nuclear dust. Component C displays a colour index of $W1 - W2 \ll 0.8$ (Vega mag). Falling significantly below the robust AGN selection threshold defined by Stern et al. (2012), this metric implies that the infrared emission is dominated by stellar light rather than an active nucleus.

Complementing this photometric view, the optical spectrum lacks the characteristic broad emission lines, specifically $H\alpha$ or $H\beta$, associated with Type I AGN. The observed narrow emission lines are weak and consistent with ionisation by hot, massive stars rather than hard X-ray ionisation fields. We must also address the potential presence of severely obscured Type II AGN. Although dust tori attenuate ultraviolet and optical photons, re-

processing dictates that this energy is inevitably re-emitted as thermal radiation in the mid-infrared (Assef et al. 2013). Consequently, the colour indices of $W1 - W2$ remain effective diagnostics to rule out Type II AGN. While we cannot strictly exclude weak, inefficient Low-Ionisation Nuclear Emission-line Regions (LINERs), the lack of a significant mid-infrared excess renders radiation-dominated AGN highly unlikely to be the primary driver of the observed ultraviolet activity (Yan & Blanton 2012).

4.3.2. UV Upturn

Massive, quiescent ETGs commonly exhibit a “UV upturn”, which is a rise in flux shortward of 2500 \AA attributed to old, hot helium-burning horizontal branch (HB) populations, rather than young stars (O’Connell 1999; Yi et al. 1998). Disentangling this evolved population from genuine recent star formation, we analysed the locus of Component C on the $NUV - r$ versus $r - K_s$ colour–colour diagram (see Figure 8).

To mitigate the age-dust degeneracy inherent in optical colours and accurately characterise the evolutionary state of Component C, we employ the NUVrK diagnostic diagram (Arnouts et al. 2013) presented in Figure 8. The star-forming “Blue Cloud” and the transitional “Green Valley” are defined by the colour ranges $1 < NUV - r < 3$ and $3 < NUV - r < 5.4$, respectively, largely following the bimodal distribution of local galaxies derived by Wyder et al. (2007). Conversely, the quiescent Red Sequence is strictly defined by colours redder than $NUV - r \geq 5.4$, a criterion extensively employed in the statistical analysis of ETGs (Schawinski et al. 2007; Kaviraj et al. 2007). This specific threshold is physically anchored to ultraviolet observations of NGC 4552, a classical elliptical galaxy identified by Burstein et al. (1988) with a UV colour of 5.4. Crucially, this system exhibits the strongest known UV upturn driven purely by evolved horizontal branch stars. As noted by Schawinski et al. (2007), $NUV - r = 5.4$ therefore represents an empirical limit for the blueness of an old stellar population; any system significantly bluer than this boundary implies a contribution from young, massive stars rather than solely evolved populations.

With an observed colour of $NUV - r \sim 4.3$, Component C resides firmly within the Green Valley, falling significantly below the quiescent threshold. Such a pronounced UV excess cannot be attributed to the classical UV upturn alone, thereby supporting the scenario of a massive galaxy undergoing low-level star formation.

4.3.3. Gas Stripping and Group Pre processing

As a massive elliptical galaxy, Component C belongs to a population typically depleted of intrinsic cold gas (e.g. Young et al. 2011). Consequently, the requisite fuel driving the observed rejuvenation likely stems from an external source (Kaviraj et al. 2007; Chauke et al. 2019). A detailed inspection of the immediate environment reveals no evidence of gas-rich dwarf satellites, effectively discounting a minor merger with a faint companion as the driver. Furthermore, internal secular evolution is effectively ruled out by the prolonged ~ 6 Gyr quiescent epoch derived from our SFH analysis. Given that dust grains in hot halos are rapidly destroyed via thermal sputtering on timescales of $\tau_{\text{sputt}} \lesssim 10^8$ yr (significantly shorter than the quiescent period; e.g. Clemens et al. 2010), the observed substantial ISM cannot be a remnant from the distant past and may be recently acquired. With alternative intrinsic and minor-merger channels excluded, we posit the

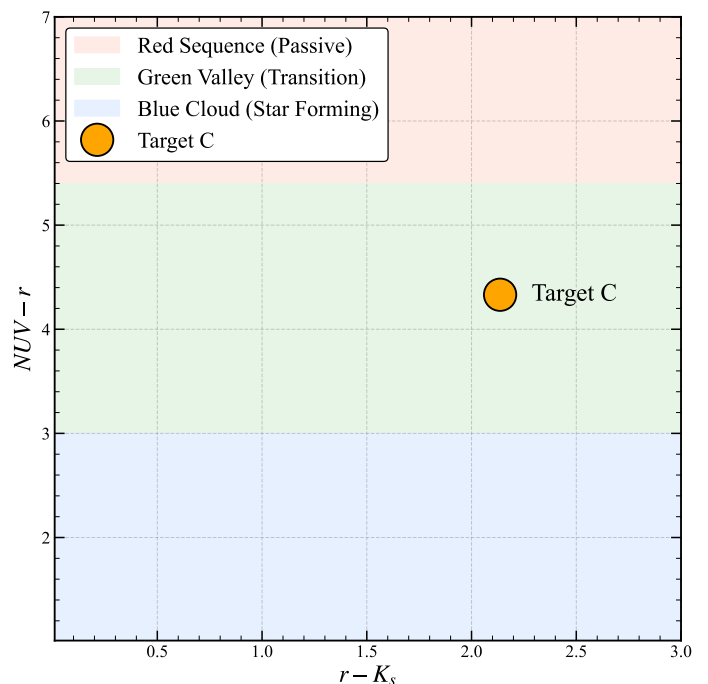


Fig. 8. The $NUV - r$ versus $r - K_s$ colour–colour diagram. Component C, marked with a red circle, resides in the Green Valley ($3 < NUV - r < 5.4$), distinguishing it from the Red Sequence ($NUV - r > 5.4$) and the Blue Cloud ($NUV - r < 3$). Error bars are plotted, but are smaller than the symbol size.

interaction with the gas-rich AB pair as the primary reservoir for the accreted material.

Unlike a transient, high-speed fly-by (e.g. Sinha & Holley-Bockelmann 2013), the tight projected separation (< 50 kpc) coupled with a substantial stellar mass ratio ($(M_A + M_B)/M_C \sim 0.4$) necessitates strong dynamical friction. Such conditions indicate a gravitationally bound system destined for a rapid merger (Boylan-Kolchin et al. 2008). In this scenario, we propose that Component C is undergoing ‘pre-processing’ during the early stages of group assembly (Fujita 2004). Driven by the major merger of the satellite pair, Components A and B, tidal forces eject substantial quantities of metal-enriched gas into the intra-group medium (Toomre & Toomre 1972; Duc & Renaud 2013). Captured by the deep gravitational potential of the massive host, this stripped material subsequently cools and settles, fuelling the observed star formation activity.

Such a gas transfer scenario effectively reconciles the apparent paradox of a “red and dead” morphology hosting a young stellar component, obviating the need for an immediate major merger event. While precise transverse velocities required to complement radial velocity measurements remain beyond the sensitivity limits of current *Gaia* astrometry for extended sources at $z \sim 0.14$ (Gaia Collaboration et al. 2018), estimates of the dynamical mass suggest the system is strongly gravitationally bound. Based on the host’s stellar mass ($M_* \approx 5.4 \times 10^{10} M_\odot$) and standard stellar-to-halo mass relations (e.g. Behroozi et al. 2013; Moster et al. 2013), we derive a virial radius of $R_{200} \approx 250$ kpc. The small projected separation of the satellites (~ 46 kpc $< 0.2R_{200}$) places them deep within the host’s potential well, effectively ruling out a transient high-speed fly-by scenario. Consequently, this dynamical configuration, combined with distinct chemical and temporal signatures of the starburst, strongly cor-

roborates the physical association. J1611+4026 thus captures an evolutionary snapshot of how interactions between satellite galaxies can indirectly rejuvenate a massive host through tidal gas stripping, preceding the eventual coalescence of the system. We acknowledge that our analysis relies on indirect tracers, specifically spatial distribution, dust, and metallicity, rather than direct imaging of the cold gas. Conclusive verification may require deeper imaging with the *James Webb Space Telescope* (JWST; Gardner et al. 2006) or dedicated gas observations using the *Atacama Large Millimeter/submillimeter Array* (ALMA; Wootten & Thompson 2009).

5. Summary

In this work, we present a comprehensive multi-wavelength analysis of J1611+4026, a unique triple system analogous to MW-LMC-SMC hierarchy. Combining spectroscopy from DESI and P200 with deep imaging from DESI-LS, we utilised GALIGHT for photometric decomposition, CIGALE for SED fitting, and BAGPIPES for full spectrophotometric fitting to characterise the physical properties, dynamical configuration, and SFH of the system. The principal findings are summarised as follows:

1. Active interaction between the satellite galaxies. Morphological decomposition via GALIGHT revealed a significant asymmetric structure extending from Component A, characterised by a significance exceeding 8σ and a spatial extent of approximately 15.15 kpc. This tidal feature provides direct morphological evidence of ongoing gravitational interaction between Components A and B. Spectroscopic and SED analyses confirmed that both satellites are gas-rich, star-forming galaxies lying above the SFMS at $z \sim 0.14$, displaying metallicity signatures consistent with an interacting state.
2. Minor rejuvenation in the massive host. Although Component C is morphologically and spectroscopically classified as a typical massive quiescent galaxy. However, multi-wavelength analysis revealed substantial internal dust extinction $E(B-V) \sim 0.53$ and a distinct NUV excess. Reconstructing the SFH via joint spectrophotometric fitting with BAGPIPES uncovered a bimodal distribution: the vast majority of stellar mass formed at $z > 1$, followed by a prolonged quiescent epoch lasting ~ 6 Gyr and subsequently punctuated by a sharp burst of star formation within the last ~ 100 Myr.
3. Quantifying the characteristics of minor rejuvenation. Our models tightly constrained the magnitude of this recent burst, yielding a negligible contribution to the total stellar mass ($f_{\text{burst}} < 0.1$ per cent). This extremely low fraction, combined with our analysis of the $NUV-r$ vs $r-K_s$ diagram and WISE mid-infrared colour diagnostics, effectively precludes the classical UV upturn or strong AGN activity as drivers of the observed anomalies. Consequently, Component C is experiencing a star formation event confined to its surface, specifically comprising a veneer of young stars contributing negligible mass superimposed onto a dominant, ancient bulge.
4. Gas accretion driven by group dynamics. Given the prolonged quiescence and current isolation of Component C, the cold gas required for rejuvenation likely has an external origin. Based on the tight spatial configuration, notably a projected separation < 60 kpc, and the active dynamical state of the satellites, we propose that rejuvenation is triggered by the accretion of metal-enriched gas stripped from the interacting AB pair. This scenario is further corroborated by metallicity dilution observed in Component A.
5. An extragalactic analogue to the MW-LMC-SMC system. J1611+4026 displays striking morphological and dynamical similarities to the local hierarchy comprising the MW, LMC, and SMC. Serving as an extragalactic analogue, this system offers a global perspective that circumvents the “inside” and “outside” observational constraints inherent to Local Group studies. The burst mass fraction measured in Component C, specifically < 0.1 per cent, establishes a quantitative benchmark; this indicates that while such satellite interactions are dynamically significant, they primarily induce localised star formation activity in the host galaxy rather than driving fundamental structural transformations.

In summary, J1611+4026 system presents an archetypal case study of how satellite interactions in group environments drive the minor rejuvenation of massive galaxies via gas stripping and re-accretion. Future high-resolution observations, specifically molecular gas mapping with ALMA, are crucial to directly image the gas transfer predicted by our models, thereby spatially resolving the kinematic connection between the interacting satellites and the rejuvenated host.

Data availability

The optical images used in this article are available on the DESI Legacy Imaging Surveys website (<https://www.legacysurvey.org/>).

Acknowledgements. We acknowledge support by the National Natural Science Foundation of China (No. 12473021), the National Key R&D Program of China (No. 2024YFA1611602), and the Key Laboratory of Survey Science of Yunnan Province (No. 202449CE340002). The author thanks Prof. Xuheng Ding for helping with running CIGALE, and thanks to Yijun Wang for her help with better cartography. The author thanks Xingyu Zhu for the photometry redshift assistance provided earlier. The Legacy Surveys consist of three individual and complementary projects: the Dark Energy Camera Legacy Survey (DECaLS), the Beijing-Arizona Sky Survey (BASS), and the Mayall z-band Legacy Survey (MzLS). DECaLS, BASS, and MzLS together include data obtained, respectively, at the Blanco telescope, Cerro Tololo Inter-American Observatory, NSF’s NOIRLab; the Bok telescope, Steward Observatory, University of Arizona; and the Mayall telescope, Kitt Peak National Observatory, NOIRLab. The Legacy Surveys imaging of the DESI footprint is supported by the Director, Office of Science, Office of High Energy Physics of the U.S. Department of Energy under Contract No. DE-AC02-05CH1123, by the National Energy Research Scientific Computing Center, a DOE Office of Science User Facility under the same contract; and by the U.S. National Science Foundation, Division of Astronomical Sciences under Contract No. AST-0950945 to NOAO. Observations were obtained with the Hale Telescope at Palomar Observatory. This work is supported by the Telescope Access Program (TAP), which has been funded by the National Astronomical Observatories of China, the Chinese Academy of Sciences, and the Special Fund for Astronomy from the Ministry of Finance. This work made use of the code CIGALE (Code Investigating GALaxy Emission; Boquien et al. 2019). We acknowledge the use of the BAGPIPES code (Bayesian Analysis of Galaxies for Physical Inference and Parameter Estimation; Carnall et al. 2018).

References

- Arnouts, S., Le Floch, E., Chevillard, J., et al. 2013, *A&A*, 558, A67
 Assef, R. J., Stern, D., Kochanek, C. S., et al. 2013, *ApJ*, 772, 26
 Barnes, J. E. & Hernquist, L. 1996, *ApJ*, 471, 115
 Behroozi, P. S., Wechsler, R. H., & Conroy, C. 2013, *ApJ*, 770, 57
 Besla, G., Kallivayalil, N., Hernquist, L., et al. 2007, *ApJ*, 668, 949
 Besla, G., Kallivayalil, N., Hernquist, L., et al. 2012, *MNRAS*, 421, 2109
 Birrer, S., Shajib, A., Gilman, D., et al. 2021, *The Journal of Open Source Software*, 6, 3283
 Bland-Hawthorn, J. & Gerhard, O. 2016, *ARA&A*, 54, 529
 Boquien, M., Burgarella, D., Roehlly, Y., et al. 2019, *A&A*, 622, A103
 Boylan-Kolchin, M., Ma, C.-P., & Quataert, E. 2008, *MNRAS*, 383, 93
 Bruzual, G. & Charlot, S. 2003, *MNRAS*, 344, 1000
 Burstein, D., Bertola, F., Buson, L. M., Faber, S. M., & Lauer, T. R. 1988, *ApJ*, 328, 440

- Calzetti, D., Armus, L., Bohlin, R. C., et al. 2000, *ApJ*, 533, 682
- Carnall, A. C., McLure, R. J., Dunlop, J. S., et al. 2019, *MNRAS*, 490, 417
- Carnall, A. C., McLure, R. J., Dunlop, J. S., & Davé, R. 2018, *MNRAS*, 480, 4379
- Casey, C. M. 2012, *MNRAS*, 425, 3094
- Cautun, M., Deason, A. J., Frenk, C. S., & McAlpine, S. 2019, *Monthly Notices of the Royal Astronomical Society*, 483, 2185
- Chambers, K. C., Magnier, E. A., Metcalfe, N., et al. 2016, *arXiv e-prints*, arXiv:1612.05560
- Chauke, P., van der Wel, A., Pacifici, C., et al. 2019, *ApJ*, 877, 48
- Chen, Q., Jing, L., Zhu, X., et al. 2025, *arXiv e-prints*, arXiv:2504.17777
- Clemens, M. S., Jones, A. P., Bressan, A., et al. 2010, *A&A*, 518, L50
- Conroy, C. 2013, *ARA&A*, 51, 393
- Davis, T. A., Alatalo, K., Sarzi, M., et al. 2011, *MNRAS*, 417, 882
- Davis, T. A., Greene, J. E., Ma, C.-P., et al. 2019, *MNRAS*, 486, 1404
- DESI Collaboration et al. 2025, *arXiv e-prints*, arXiv:2503.14745
- Dey, A., Schlegel, D. J., Lang, D., et al. 2019, *AJ*, 157, 168
- Ding, X., Onoue, M., Silverman, J. D., et al. 2023, *Nature*, 621, 51
- Ding, X., Silverman, J., Treu, T., et al. 2020, *ApJ*, 888, 37
- Duc, P.-A. & Renaud, F. 2013, in *Lecture Notes in Physics*, Berlin Springer Verlag, ed. J. Souchay, S. Mathis, & T. Tokieda, Vol. 861, 327
- Ellison, S. L., Mendel, J. T., Patton, D. R., & Scudder, J. M. 2013, *MNRAS*, 435, 3627
- Ellison, S. L., Patton, D. R., Simard, L., & McConnachie, A. W. 2008, *AJ*, 135, 1877
- Ellison, S. L., Patton, D. R., Simard, L., et al. 2010, *MNRAS*, 407, 1514
- Flesch, E. W. 2023, *The Open Journal of Astrophysics*, 6, 49
- Fox, A. J., Wakker, B. P., Barger, K. A., et al. 2014, *ApJ*, 787, 147
- Fu, Y. 2021, QSOFITMORE: a python package for fitting UV-optical spectra of quasars, Zenodo
- Fu, Y., Wu, X.-B., Jiang, L., et al. 2022, *ApJS*, 261, 32
- Fujita, Y. 2004, *PASJ*, 56, 29
- Gaia Collaboration, Brown, A. G. A., Vallenari, A., et al. 2018, *A&A*, 616, A1
- Gaia Collaboration, Vallenari, A., Brown, A. G. A., et al. 2023, *A&A*, 674, A1
- Gardner, J. P., Mather, J. C., Clampin, M., et al. 2006, *Space Sci. Rev.*, 123, 485
- Herpich, F., Stasińska, G., Mateus, A., Vale Asari, N., & Cid Fernandes, R. 2018, *MNRAS*, 481, 1774
- Hopkins, P. F., Bundy, K., Croton, D., et al. 2010, *ApJ*, 715, 202
- Hopkins, P. F., Hernquist, L., Cox, T. J., et al. 2006, *ApJS*, 163, 1
- Kallivayalil, N., van der Marel, R. P., Besla, G., Anderson, J., & Alcock, C. 2013, *ApJ*, 764, 161
- Kaviraj, S. 2014, *MNRAS*, 437, L41
- Kaviraj, S., Schawinski, K., Devriendt, J. E. G., et al. 2007, *ApJS*, 173, 619
- Kennicutt, Jr., R. C. 1998, *ARA&A*, 36, 189
- Lang, D. 2014, *AJ*, 147, 108
- Larson, K. L., Sanders, D. B., Barnes, J. E., et al. 2016, *ApJ*, 825, 128
- Lian, J., Thomas, D., Maraston, C., et al. 2018, *MNRAS*, 474, 1143
- Liang, S., Yang, W. G., Zheng, Y. G., & Kang, S. J. 2025, *ApJS*, 278, 11
- Lotz, J. M., Jonsson, P., Cox, T. J., et al. 2011, *ApJ*, 742, 103
- Martin, D. C., Fanson, J., Schiminovich, D., et al. 2005, *ApJ*, 619, L1
- Moster, B. P., Naab, T., & White, S. D. M. 2013, *MNRAS*, 428, 3121
- Naab, T., Johansson, P. H., & Ostriker, J. P. 2009, *ApJ*, 699, L178
- Neistein, E., van den Bosch, F. C., & Dekel, A. 2006, *MNRAS*, 372, 933
- Noll, S., Burgarella, D., Giovannoli, E., et al. 2009, *A&A*, 507, 1793
- O'Connell, R. W. 1999, *ARA&A*, 37, 603
- Oke, J. B. & Gunn, J. E. 1982, *PASP*, 94, 586
- Pandey, D., Kaviraj, S., Saha, K., & Sharma, S. 2024, *MNRAS*, 531, 2223
- Pang, Y., Wu, X.-B., Fu, Y., et al. 2025, *ApJ*, 980, 223
- Patton, D. R., Torrey, P., Ellison, S. L., Mendel, J. T., & Scudder, J. M. 2013, *MNRAS*, 433, L59
- Popesso, P., Concas, A., Cresci, G., et al. 2023, *MNRAS*, 519, 1526
- Renzini, A. 2006, *ARA&A*, 44, 141
- Rix, H.-W. & Bovy, J. 2013, *A&A Rev.*, 21, 61
- Rowlands, K., Dunne, L., Maddox, S., et al. 2012, *MNRAS*, 419, 2545
- Salpeter, E. E. 1955, *ApJ*, 121, 161
- Salvador-Rusiñol, N., Vazdekis, A., La Barbera, F., et al. 2020, *Nature Astronomy*, 4, 252
- Sanders, D., Soifer, B., & Neugebauer, G. 1990, in *Dynamics and Interactions of Galaxies: Proceedings of the International Conference, Heidelberg, 29 May–2 June 1989*, Springer, 459–464
- Sanders, D. B., Soifer, B. T., Elias, J. H., et al. 1988, *ApJ*, 325, 74
- Schawinski, K., Thomas, D., Sarzi, M., et al. 2007, *MNRAS*, 382, 1415
- Schlafly, E. F., Meisner, A. M., & Green, G. M. 2019, *ApJS*, 240, 30
- Schreiber, C., Pannella, M., Elbaz, D., et al. 2015, *A&A*, 575, A74
- Scudder, J. M., Ellison, S. L., Torrey, P., Patton, D. R., & Mendel, J. T. 2012, *MNRAS*, 426, 549
- Sinha, M. & Holley-Bockelmann, K. 2013, *Asociacion Argentina de Astronomia La Plata Argentina Book Series*, 4, 120
- Skrutskie, M. F., Cutri, R. M., Stiening, R., et al. 2006, *AJ*, 131, 1163
- Stalevski, M., Ricci, C., Ueda, Y., et al. 2016, *MNRAS*, 458, 2288
- Stern, D., Assef, R. J., Benford, D. J., et al. 2012, *ApJ*, 753, 30
- Stierwalt, S., Besla, G., Patton, D., et al. 2015, *ApJ*, 805, 2
- Toomre, A. & Toomre, J. 1972, *ApJ*, 178, 623
- Trager, S. C., Faber, S. M., Worthey, G., & González, J. J. 2000, *AJ*, 120, 165
- Wang, Y., Wang, T., Xu, K., et al. 2025, *ApJ*, 980, 107
- Werle, A., Cid Fernandes, R., Vale Asari, N., et al. 2020, *MNRAS*, 497, 3251
- Wooten, A. & Thompson, A. R. 2009, *IEEE Proceedings*, 97, 1463
- Wright, E. L., Eisenhardt, P. R. M., Mainzer, A. K., et al. 2010, *AJ*, 140, 1868
- Wyder, T. K., Martin, D. C., Schiminovich, D., et al. 2007, *ApJS*, 173, 293
- Yan, R. & Blanton, M. R. 2012, *ApJ*, 747, 61
- Yi, S., Demarque, P., & Oemler, Jr., A. 1998, *ApJ*, 492, 480
- Yi, S. K., Yoon, S.-J., Kaviraj, S., et al. 2005, *ApJ*, 619, L111
- Young, L. M., Bureau, M., Davis, T. A., et al. 2011, *MNRAS*, 414, 940

Appendix A: Spectrum fitting by `qsOFITMORE`

The `qsOFITMORE` fitting results of Component A, B, and C are shown in [Fig. A.1](#), [Fig. A.2](#), and [Fig. A.3](#), respectively.

Appendix B: Posterior Analysis with BAGPIPES

We present the joint posterior probability distribution derived from our independent BAGPIPES analysis to demonstrate the robustness of the derived dust attenuation and to explicitly rule out the age–dust degeneracy discussed in [Section 4.2](#).

Appendix C: SED model parameter

We present the detailed input parameters and their corresponding ranges adopted for the SED fitting with CIGALE.

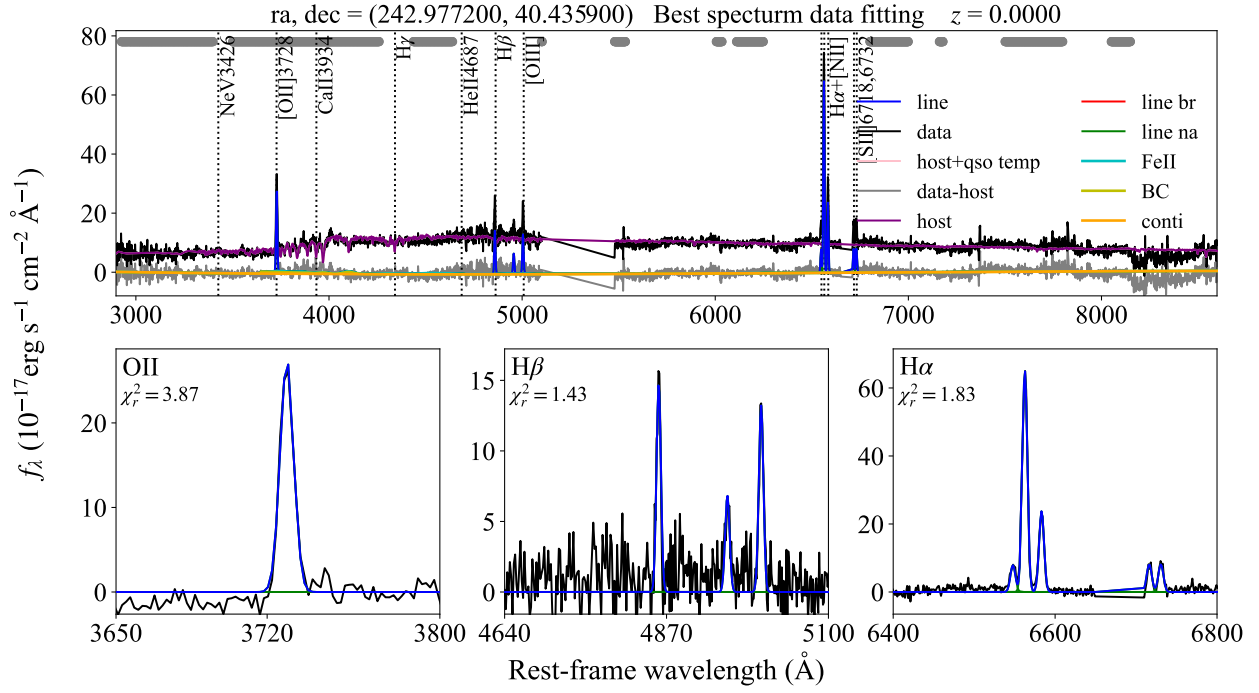


Fig. A.1. QSOFITMORE spectroscopic fitting of J1611+4026A. Upper panel: The fitting of the full spectrum considering the subtraction of the host component. Spectral regions covering 5105–5478 Å and 6650–6710 Å were masked during the fitting procedure to exclude mechanical failure and telluric absorption features, respectively. $z=0$ means the spectrum has already been corrected for redshift. Lower panels: Zoom-in on the fitting of H_α and H_β .

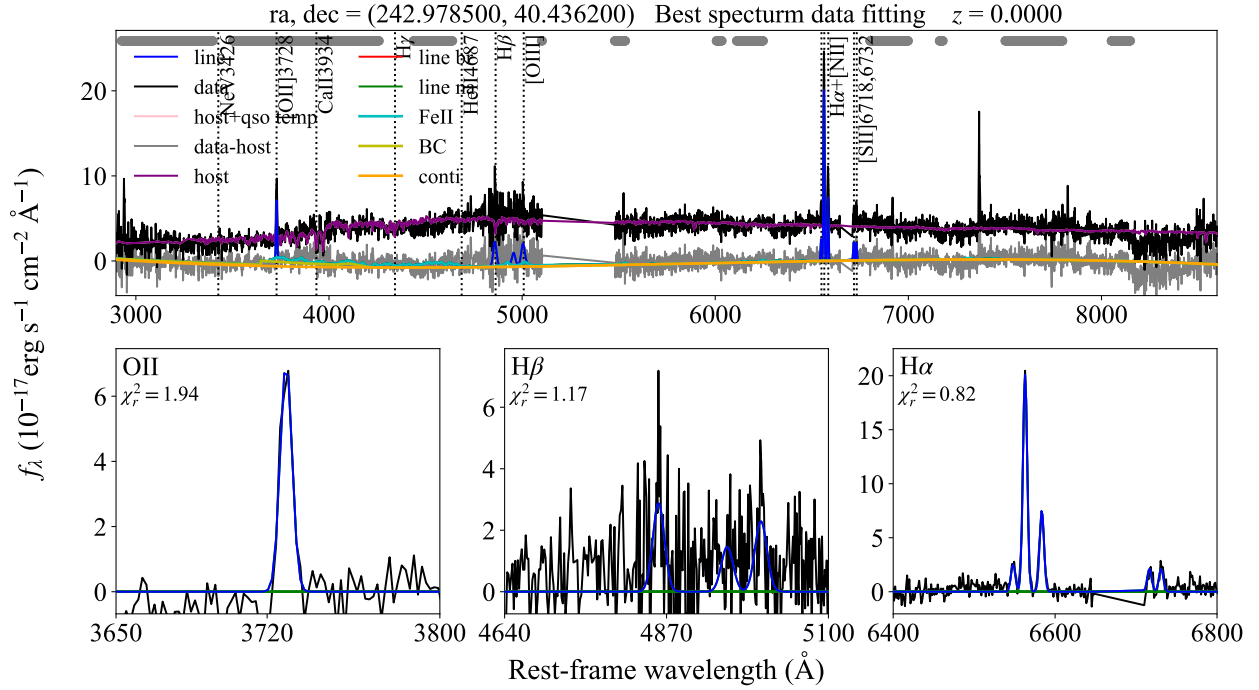


Fig. A.2. Same as Fig. A.1, but for J1611+4026B.

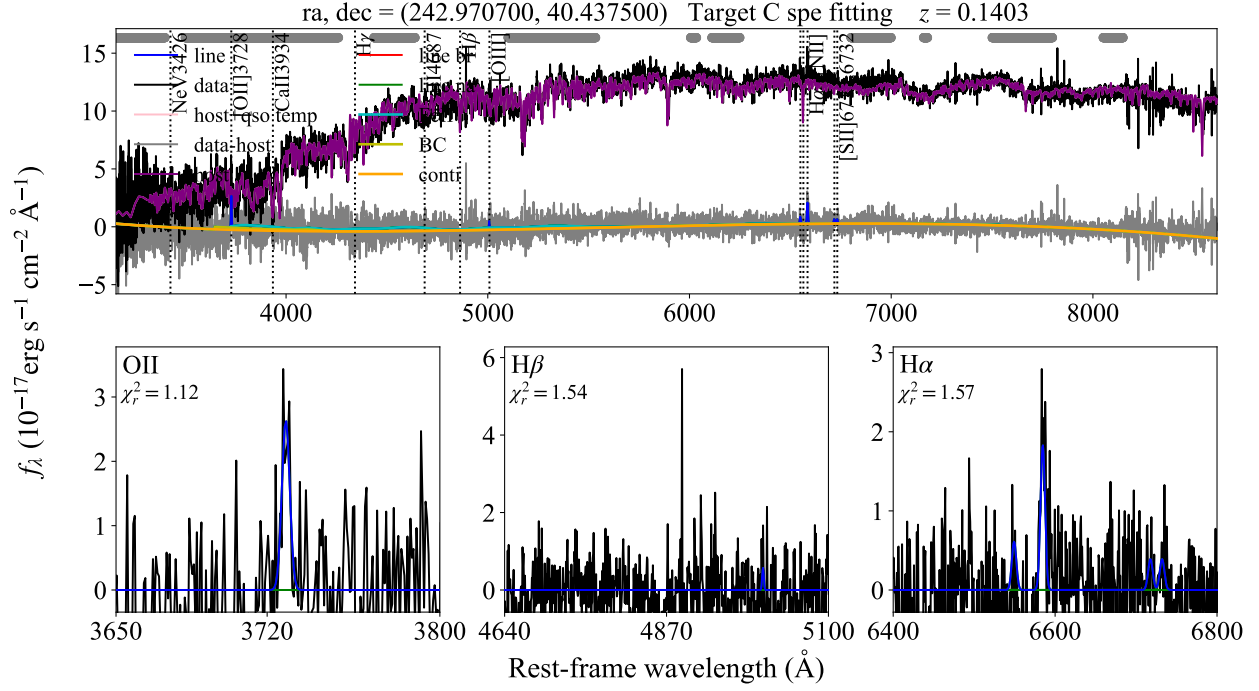


Fig. A.3. Same as Fig. A.1, but for J1611+4026C.

Table C.1. Input parameters for the SED fitting with CIGALE.

Module	Parameter	Symbol	Values
Star formation history (Delayed SFH + Burst/Quench)	e-folding time of main population	τ_{main} (Myr)	1000, 2000, 3000, 5000, 8000
	Age of main population	t_{main} (Myr)	2000, 5000, 8000, 10000
	Age of burst/quench episode	t_{burst} (Myr)	5, 10, 20, 50, 100, 300, 500, 1000
Simple stellar population (Bruzual & Charlot 2003)	Initial mass function	IMF	(Salpeter 1955)
	Metallicity	Z	0.02 (Z_{\odot}), 0.05
Dust attenuation (Calzetti et al. 2000)	Color excess of nebular lines	$E(B - V)_{\text{lines}}$ (mag)	0.05, 0.1, 0.2, ..., 0.9
	Stellar continuum factor	f_{att}	0.44
Dust emission (Casey 2012)	Dust Temperature	T_{dust} (K)	20, 25, 30, 35, 40, 45, 50
	Emissivity index	β	1.6
	MIR power law slope	α	2.0
AGN emission (SKIRTOR, Stalevski et al. 2016)	AGN fraction	f_{AGN}	0.0, 0.02, 0.05, 0.1, ..., 0.99
	Viewing angle	i (deg)	30, 70
	Optical depth ($9.7 \mu\text{m}$)	$\tau_{9.7}$	3, 5, 7

Notes. $f_{\text{att}} = E(B - V)_* / E(B - V)_{\text{lines}}$.

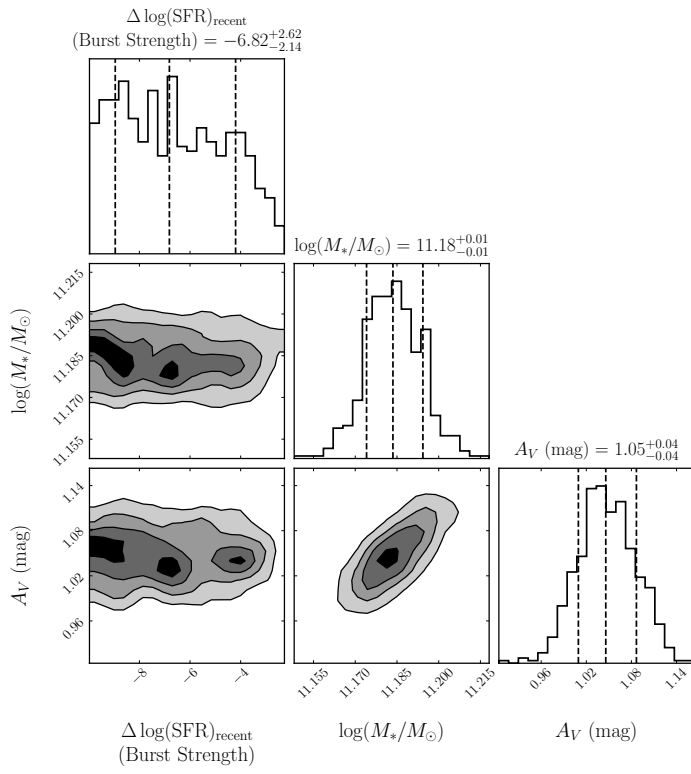


Fig. B.1. Posterior distributions for recent star formation strength, stellar mass, and dust attenuation (A_V) from BAGPIPES. Dashed lines indicate the median and 1σ intervals. The lack of covariance between A_V and $\Delta \log(\text{SFR})_{\text{recent}}$ (bottom-left) confirms that the derived extinction is robust and not degenerate with the rejuvenation signal.